Journal of Nuclear Materials 481 (2016) 147–152

Contents lists available at ScienceDirect

Journal of Nuclear Materials

journal homepage: www.elsevier.com/locate/jnucmat

Self-interstitials structure in the hcp metals: A further perspective from first-principles calculations

Roberto C. Pasianot [a, b, c, *]

[a] Gerencia Materiales, CAC-CNEA, Avda. Gral. Paz 1499, 1650 San Martín, Argentina
[b] CONICET, Godoy Cruz 2290, 1425 Buenos Aires, Argentina
[c] Instituto Sabato, UNSAM/CNEA, Avda. Gral. Paz 1499, 1650 San Martín, Argentina

ARTICLE INFO

Article history:
Received 27 April 2016
Received in revised form
26 August 2016
Accepted 19 September 2016
Available online 20 September 2016

Keywords:
SIA structure
HCP metals
First-principles calculations

ABSTRACT

We study the structure of several standard and non-standard self-interstitial configurations in a series of hcp metals, by using Density Functional Theory as embodied in the computer codes SIESTA and WIEN2k. The considered metals include Be, Mg, Ti, Zr, Co, Zn, and Cd, thus spanning the whole range of experimental c/a ratios, different kinds of bonding, and even magnetism (Co). The results show the importance of low symmetry configurations, closely related to the non-basal crowdion, in order to rationalize the experimental data on self-interstitial structure and migration.

1. Introduction

Proper knowledge of the self-interstitial structure in metals is essential for the understanding of how those metals change their microstructure, e. g. when exposed to irradiation environments or while undergoing heavy mechanical work. Microstructure evolution impacts chiefly the mechanical properties and may thus become a critical issue for in-vessel components of nuclear reactors. From a fundamental perspective, knowledge of this kind informs the modeling of irradiation effects in solids, subject initiated in the 1950s, that has received renewed interest in more recent times, as witnessed for instance in the COSIRES series of conferences. Among these modelings, worth of noticing are the ones aimed at producing tools for the assessment of power plant life extension, motivated by the many plants worldwide that nowadays are approaching their planned end of life. A few examples along these lines are efforts undertaken in the framework of several recent projects, such as REVE [1], PERFORM 60 [2], and PERFECT [3].

Within this context, the application of the Density Functional Theory (DFT), that has taken place in the past 15 years or so, to study the structure of defects and their interactions with impurities, represents a major step. Both, the wider availability of codes and the increase (and availability) of computing power, contributed to make it possible. Focusing on the interstitial defect, DFT was able, for instance, to provide a consistent picture of the structure across the bcc transition metals of the periodic chart [4,5], where the <110> and <111> dumbbells compete for the lowest energy configuration. In particular, the experimentally observed [6] <110> structure in Fe, somewhat off-trend from theoretical expectations, was explained as due to magnetic effects, and even reasonable quantitative agreement with experiment was obtained for the kinetics of irradiation recovery [7].

The situation regarding the hcp metals, however, is less satisfactory. In a former work by the present authors [8], an interatomic potential for Zr of the Embedded Atom Method (EAM [9]) kind, was carefully fitted to available experimental data, and applied to simulating some defect structures. It was predicted that six of the assumed standard interstitial configurations for the hcp lattice, had formation energy within 0.3 eV. Moreover, the reported lowest energy configuration, basal split (Bs), showing one-dimensional (1D) migration at low temperatures [10] (though switching gradually to 3D at higher ones), might not be entirely consistent with experiments. However, we also pointed out that experiments carry some degree of conflict. Internal friction (IF) measurements after neutron irradiation at liquid Nitrogen temperatures favor a defect

* Gerencia Materiales, CAC-CNEA, Avda. Gral. Paz 1499, 1650 San Martín, Argentina.
E-mail address: pasianot@cnea.gov.ar.

http://dx.doi.org/10.1016/j.jnucmat.2016.09.021
0022-3115/

with a monoclinic elastic dipole [11], whereas Huang diffuse X-rays scattering (DXS) after electron irradiation at liquid Helium temperatures is consistent with a dipole isotropic on the basal plane [12], though other possible symmetries cannot be ruled out. A later theoretical study on Zr [13], this time applying the DFT methodology implemented in the VASP code [14], reported five configurations with formation energy within 0.24 eV, though not the same set as before and not in the same order of energies. Besides, the predicted most stable structure, octahedral (O), is not responsive to internal friction. A more recent study on Zr [15], also using VASP but employing larger simulation cells (up to 288 hcp sites against former 96), reported the basal octahedral (Bo) as the most stable configuration, closely followed by Bs and then O. This preference for basal structures suggests a defect that will mainly diffuse in 2D; besides, even though Bs responds to internal friction, it does not posses monoclinic symmetry. To essentially the same results arrived a further study [16] where both codes, VASP and SIESTA [17], were used; this is after discarding their reported, low-symmetry, BC′ configuration which was later shown to have a negligible barrier for decaying to Bo [18]. Interestingly, ref. [16] also reports another low-symmetry configuration that possesses a screw-like structure along the *c* axis (PS-C′) and a very flat energy profile; this ought to migrate along the *c* axis almost athermally but, lying about 0.25 eV above Bo, it would take some thermal activation to be significantly populated.

Here we undertake to study the structure of standard (assumed) and non-standard self-interstitial atoms (SIA) for a range of hcp metals, comprising Be, Mg, Ti, Zr, Co, Zn, and Cd. Thus, a relatively large variation in the *c*/*a* ratio is explored, as well as different types of bonding. The main aim is to gain insight on the possible migration mechanisms, on a wider perspective than group *IV* B metals, to be tested against the (limited) experimental data. The methodology, based on the application of DFT, is explained in sec. 2 below; results together with the discussion and comparison with experiments, are reported in sec. 3; finally, sec. 4 is devoted to the conclusions, also including a brief summary of the main findings.

2. Methodology

The calculation procedure consists on the sequential application of two DFT codes: i) SIESTA [17] (ver.3.0), which is based on pseudopotentials and numerical, strictly localized, atomic-like basis functions for wave-functions expansion, and ii) the all-electron, full-potential, WIEN2k code [19] (ver.12.1), which implements the Augmented Plane Wave plus Local Orbitals technique, in order to expand the wave-functions, thus more accurate but also requiring much more computational resources than the former. Final energies of the tested configurations are taken from the output of the latter code, in order to assure maximum reliability for the simulation supercell size employed; this is limited to 96 hcp sites ($4 \times 4 \times 3$ repeated hexagonal cells). Though this supercell size has been used in previous works, e.g. Ref. [13], it has later been shown [15] that for SIA configurations falling very close in formation energy, cells about twice as large may be needed to get the correct energy ordering. Our arguments, however, are qualitative in nature, based on identifying groups of configurations of lowest energy and analyzing their structures. Even though larger simulation cells may be necessary to reveal the fine details of energy ordering within such groups, the groups themselves are correctly captured by our present methodology.

In short, firstly each SIA configuration is handled to SIESTA for coordinates relaxation in order to minimize their energy (conjugate gradients technique) under the action of a given pseudopotential, aiming at individual forces typically below about 0.01 eV/Å. During the process, the simulation cell size and shape are kept fixed, consistent with the equilibrium lattice parameters previously determined for that same pseudopotential. Secondly, the cell energy is re-computed by using the all-electron code WIEN2k, after re-scaling to the lattice parameters determined beforehand, now with the latter code. Thirdly and eventually, a further coordinates relaxation is undertaken by using WIEN2k, as a check and for selected instances. This last step is very much expensive in computational resources than the first one (and this is the whole point of our sequential approach), but is also generally not needed within the bounds of our current purposes, because the further energy decrease typically amounts to some 0.02–0.03 eV for the whole cell, though it may vary somewhat across configurations. Thus the formation energies we consider to be representative are the ones derived from the second step. An example of the consistency of this approach is given in Table 1 for the case of Zr, where the formation energy of several SIA configurations (to be detailed later on) is reported after application of each of the three steps just mentioned. For comparison, also reported are the values from Ref. [13] for the same supercell and boundary conditions, but using the VASP code furnished with an ultrasoft pseudopotential. Moreover, on the last row we have applied the defect-defect elastic interaction correction according to Ref. [18] to step 3 results (using dipoles from SIESTA simulations and experimental elastic constants), obtaining agreement with their Fig. 3 for the same size, and almost the converged energy ordering of larger cells. Clearly, the only significant differences for our purposes are reflected in the first two rows.

More technical details regarding pseudopotentials, basis functions, and calculation parameters are as follows. Pseudopotentials are of the so called norm-conserving Troullier-Martins kind [20], build upon the PBE [21] GGA exchange and correlation functional, including relativistic effects and core charge corrections. The Zr and Ti pseudopotentials, already used in some of our previous works [22–24], were taken from SIESTA's home page. The remaining ones were build by us, using the ATOM utility bundled with the SIESTA package, mainly because of consistency reasons with the former two (GGA and core corrections). Table 2 gathers the reference electronic configurations for pseudopotential generation; also reported is the quality of the atomic-like basis functions for wave-functions expansion needed in SIESTA's method. Overall, Zr and Ti include the *s* and *p* states from the core and correspond to ionic (+2) configurations; Zn includes the complete $3d^{10}$ shell, all the rest are standard atomic ground state (valence) configurations. The (parameters of the) basis functions, that broadly can be termed as double-zeta polarized (DZP, two radial functions per *l*-angular momentum channel, plus a third, $l + 1$, orbital, polarizing the former two), were optimized for a small hcp cell with the simplex technique, checking a posteriori for reasonable match to the experimental hcp lattice parameters, while assuring stability with respect to the fcc and bcc lattices. Such a procedure failed for Cd, however, having developed the Zn case, which possesses about the same, relatively large, *c*/*a* ratio, this posed no real problem for the subsequent stage involving the WIEN2k code.

Table 1
Calculated SIA (heading row) formation energies (eV) for Zr after each of the three steps in our sequential approach.

	O	Bo	C	S	S*	Bs
Step 1 (SIESTA)	3.37	3.44	3.68	3.48	3.48	3.70
Step 2 (WIEN2k)	3.05	3.07	3.46	3.23	3.19	3.18
Step 3 (WIEN2k)	3.04	3.04	3.42	3.20	3.17	3.13
Ref. [13]	2.94	2.98	3.25	3.12	–	3.09
Step 3 corrected[a]	2.95	2.90	3.32	3.09	3.08	2.95

[a] Elastic correction according to Ref. [18].

Table 2
Reference electronic configurations for pseudopotentials generation and schematic description of corresponding SIESTA's basis functions (total number of ($l.m$) orbitals on the far right).

Element	Configuration	Basis functions
Be	$2s^2 2p^0 3d^0 4f^0$	$2s \times 2 + 2p = 5$ orb.
Mg	$3s^2 3p^0 3d^0 4f^0$	$3s \times 2 + 3p + 3d \times 2 = 15$ orb.
Ti(+2)	$3s^2 3p^6 3d^2 4f^0$	$3s + 4s \times 2 + 3p + 4p + 3d \times 2 = 19$ orb.
Zr(+2)	$4s^2 4p^6 4d^2 4f^0$	$4s \times 2 + 5s \times 2 + 4p \times 2 + 5p + 4d \times 2 = 23$ orb.
Co	$4s^2 4p^0 3d^7 4f^0$	$4s \times 2 + 4p + 3d \times 2 = 15$ orb.
Zn	$4s^2 4p^0 3d^{10} 4f^0$	$4s \times 2 + 4p + 3d \times 2 = 15$ orb.
Cd	unsuccessful	

Other relevant parameters specific to the SIESTA relaxation runs, besides those already mentioned, include: a $3 \times 3 \times 3$ reciprocal space grid (may vary somewhat from metal to metal), equivalent to about 1500 k-points in the primitive hcp cell, a 0.15 eV smearing temperature for Brillouin zone integration (Fermi-Dirac scheme), and spin-polarized calculations for Co. Regarding the WIEN2k runs, the reciprocal space grid was kept as above, the muffin-tin radii were chosen as large as possible and fixed across SIA configurations (for consistent energy comparisons), the parameter controlling the basis size, RKMAX, was set to 7 (recommended standard for most cases and still affordable), spin-polarization was set for Co, all remaining parameters took default values.

The SIA structures considered are depicted in Fig. 1; they are the octahedral, O, basal octahedral, Bo, crowdion, C, split dumbbell, S, basal split, Bs, and split skew, S*. The latter is not among the standard interstitials, it was found as a byproduct of saddle configurations searches in Zr, and then tested in the other metals because of its relatively low formation energy; also, it is very similar to the so called PS in Ref. [16]. For convenience, a unique name is given to it, though the structure details vary across metals. Standard configurations also include the tetrahedral, T, its basal projection, Bt, and basal crowdion, Bc. Common experience, however, shows that the former two possess high formation energy, while the latter is either unstable or barely distinguishable from Bs, thus none of them were simulated.

Lastly, we have also computed vacancy formation energies, E_f^V

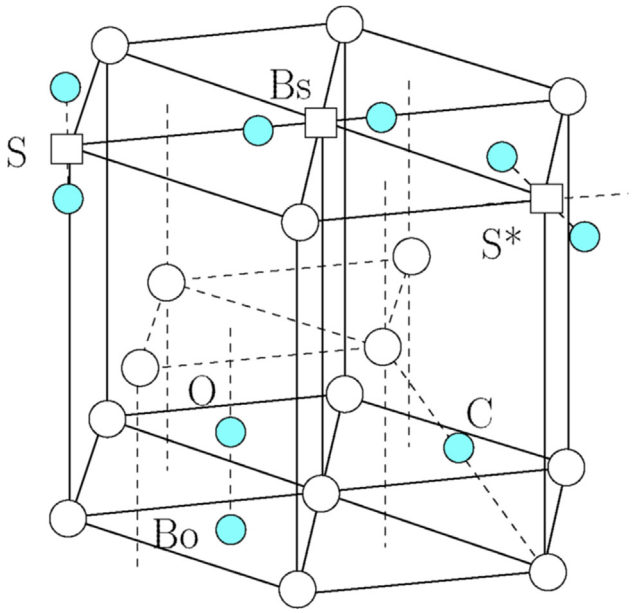

Fig. 1. Location of the simulated SIA configurations in the hcp lattice (pictorial).

(WIEN2k), SIA dipole tensors, P_{ij}, from the stresses remaining on the supercell after relaxation (SIESTA, [18]), and saddle configurations for SIA migration (SIESTA, monomer technique [25]). Because of the importance of P_{ij} in the present context, we shortly remind that the DXS technique [26] allows the measurement of certain invariant combinations (under the lattice point symmetries), the two most reported being,

$$\pi^{(1)} = P_{33}^2$$
$$\pi^{(3)} = 2\left(P_{11}^2 + P_{22}^2 + 2P_{12}^2\right) + (P_{11} + P_{22})^2 , \quad (1)$$

where axes 1 and 2 lie on the basal plane, and 3 is perpendicular to it. There are a third one, $\pi^{(2)} = (P_{13}^2 + P_{23}^2)$, unfortunately never reported, and a fourth one that substitutes $(-)$ for the central $(+)$ in $\pi^{(3)}$. On the other hand, experimental results are often presented through the anisotropy ratio, P_{33}/P_a, where $P_a = \sqrt{\pi^{(3)}/8}$, which provides some information on the defect shape, thus helping to narrow the search for possible candidates.

In summary, results of all these calculations will be quoted in the following when appropriate, noting though, that they have not been performed in a systematic manner for all the cases considered.

3. Results and discussion

Table 3 gathers all the computed SIA formation energies, E_f (from step 2 above), also shown in Fig. 2 for easier visualization, as well as some results for Zr from the literature. Before entering a case by case analysis, a few general comments are in order. Due to its constricted condition, naive hard spheres models expect Bo to be a barrier between consecutive O configurations along the c axis [28]. This is at variance with calculations, where $E_f(\mathrm{Bo}) - E_f(\mathrm{O})$ roughly correlates with the c/a ratio, most notably for Zn and Cd whose ratios depart the most from the ideal $\sqrt{8/3}$. Interestingly, however, for the cases where O and Bo are very close in energy, such as Zr and Ti, the energy landscape along the sequence OBoOBo… (envisaged as a hollow channel in the ABAB… stacking) is not flat: a barrier of about 0.15 eV (referred to Bo) was presently found for both materials. On the other hand, configuration C, in spite of being squeezed between two non-basal neighbors, can have a relatively low formation energy (Zn, Cd, Mg,…) thus suggesting a likely 3D SIA migration. Also configuration S* is, globally, a low energy SIA; this should contribute to 3D migration as well, though, as it will become clear in what follows, markedly anisotropic.

Experimental results for Be are rather scanty [6], among them, low temperature recovery stages have been measured after

Table 3
Calculated SIA formation energies (eV) for the seven hcp metals considered. Predicted all-electron (experimental) c/a ratios in the last column.

	O	Bo	C	S	S*	Bs	c/a
Be	5.19	4.15	4.58	5.44	unst.	4.29	1.571 (1.567)
Be[a]	5.24	4.20	4.39	5.29		4.30	
Mg	2.51	2.45	2.35	2.49	2.35	2.56	1.608 (1.623)
Ti	2.58	2.54	3.12	2.93	2.87	2.77	1.583 (1.587)
Zr	3.05	3.07	3.46	3.23	3.19	3.18	1.603 (1.593)
Zr[b]	2.94	2.98	3.25	3.12		3.09	
Zrc[c]	2.98	2.82	3.37	3.17		2.96	
Co	5.04	4.90	4.49	4.39	4.43	5.55	1.618 (1.623)
Zn	1.12	3.31	1.14	1.27	1.14	3.50	1.875 (1.856)
Cd	1.03	3.31	0.99	1.09	0.99	3.49	1.896 (1.886)

[a] Ref. [27], VASP, 150 sites, const. volume.
[b] Ref. [13], VASP, 96 sites, const. volume.
[c] Ref. [15], VASP, 180 sites, const. rescaled volume.

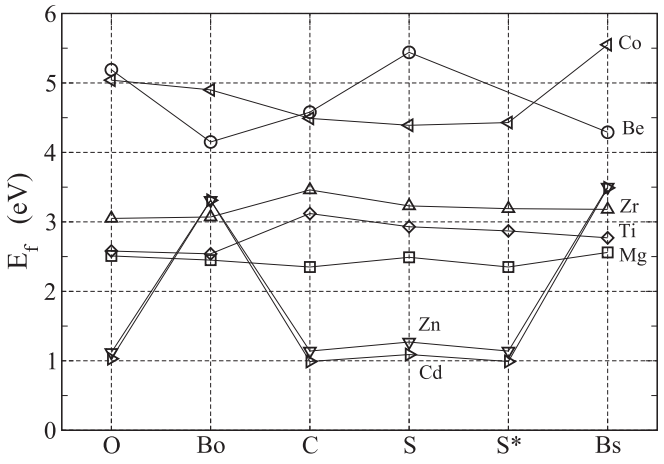

Fig. 2. Graphical representation of SIA formation energies from Table 3; lines are meant to guide the eye.

neutron irradiation. These experiments assign stage I_D to the temperature range 30–50 K, which is compatible with a migration barrier $E_m^{\mathrm{I}} \approx 0.1 - 0.2$ eV, similar to the calculated difference $E_f(\mathrm{Bs}) - E_f(\mathrm{Bo}) = 0.14$ eV. On the other hand, the difference $E_f(\mathrm{C}) - E_f(\mathrm{Bo}) \approx 0.4$ eV is too high to be relevant for such a temperature range, thus the SIA migration would essentially be 2D, involving the two basal configurations Bo and Bs. Configuration S* turned out to be unstable, decaying either to C (SIESTA) or to Bo (WIEN2k). Previous DFT calculations [27] are in reasonable agreement with the current ones in both, the rather large formation energies and the order of configurations stability (cf. Table 3); the difference $E_f(\mathrm{C}) - E_f(\mathrm{Bo}) = 0.19$ eV is somewhat smaller but also is $E_f(\mathrm{Bs}) - E_f(\mathrm{Bo}) = 0.10$ eV, so that 2D migration would still hold.

Regarding Mg, C and S* are predicted to be the lowest energy, almost degenerate, SIAs. The former keeps the (site) inversion symmetry and is well described by its three off-lattice atoms, one of them occupying the center of symmetry, with a barely noticeable S shape when seen from a $[11\bar{2}0]$ axis. S*, whose basal projection is depicted in Fig. 3, essentially comprises the same three atoms and may be thought of as a C of broken symmetry. Two of those atoms, 2 and 3, share a lattice site via a dumbbell, and the third one, 1, appears closer to a lattice position. The dumbbell lies slightly inclined with respect to the plane $\{11\bar{2}0\}$, that, being a mirror plane, leads to degeneracy. Experimentally, there is some controversy regarding recovery stage I [6], namely, interstitials would start migrating at 13 K, however there is some evidence of annealing already at 4–5 K. Also, a value of $P_{33}/P_a = 0.3 \pm 0.02$ has been obtained from DXS measurements [12]; this might be compatible with our calculated 0.30 for Bo, or even with 0.36 for Bs, all other values being larger than 1.0. However, both configurations lie at least 0.1 eV higher in energy than the former two and, moreover, the experimental ratio has been attributed to small planar prismatic clusters [12]. Thus, recovery at such low temperatures most likely involves configurations C and S*, that due to their closely related structures, should be connected by low migration barriers. In order to test this hypothesis, we calculated a symmetric dumbbell about site 0 in Fig. 3 (horizontally projected), that would connect the C configuration located midway sites 0 and 5, to the one located between sites 0 and 1. The structure was obliged to remain symmetric through forces constraints, and indeed its formation energy resulted in less than 0.01 eV above E_f(C), Notice that the same would hold if the final C were located between sites 0 and 4, entailing that migration occurs, effectively, in 3D; moreover, the easy exchange between the degenerate forms of S*, should also help in promoting 3D migration.

Experimental data on structure and diffusion of SIAs in Ti is almost non-existent [6]. The only of concern to our study is that recovery stage I has been observed after both, electron and neutron irradiation, at a temperature T_{ID} of 120–130 K, and was attributed to SIA migration. However, belonging to the same group IV B as Zr, and noting the very same trends in SIA formation energies for both species, Fig. 2, a qualitative difference with Zr behavior can hardly be expected. Thus we concentrate the discussion on the latter, where there are more data available.

Relevant experimental information for Zr includes: i) a large recovery stage I starting at a temperature $T_{ID} \approx 102$ K, attributed to SIA migration [6], ii) DXS measurements on single crystals after electron irradiation at 4.5 K report $P_{33}/P_a = 1.1 \pm 0.2$ [12], and iii) IF measurements after neutron irradiation of poly-crystals at 77 K, report a split peak, P'_1 and P_1, thus attributed to a single defect, with reorientation energies of 0.17 eV and 0.27 eV respectively, and overall migration energy $E_m^{\mathrm{I}} = 0.30$ eV [11]. On the theoretical side, all DFT calculations obtain C as the highest energy SIA, though ours turned out to be a saddle or a very shallow metastable configuration. In fact, a small displacement of the central atom perpendicular to the crowdion axis and parallel to the basal plane, leads to a buckled C structure, C*, having $E_f(\mathrm{C}^*) = 3.21$ eV, namely, only 0.02 eV higher than S*. Both SIAs are depicted by their basal projection in Fig. 4. Indeed, they have already been found in the literature by the names SP and C' [16], also noting their possible relevance to the IF experiment, though providing no analysis. The

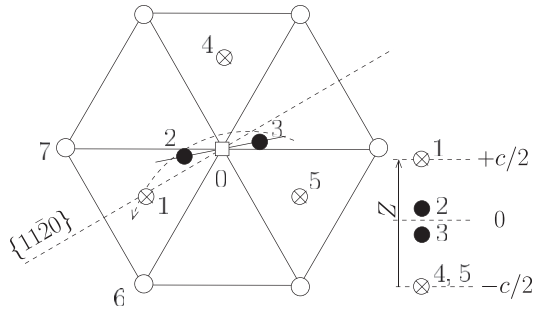

Fig. 3. Basal projection of S* SIA in Mg (schematic). Trace of $\{11\bar{2}0\}$ plane and stacking perpendicular to the paper are indicated; dashed arc suggests the curved, winding upwards, asymmetry. Atoms 6 and 7 are at $Z = 0$ level and serve later purposes (see Co case).

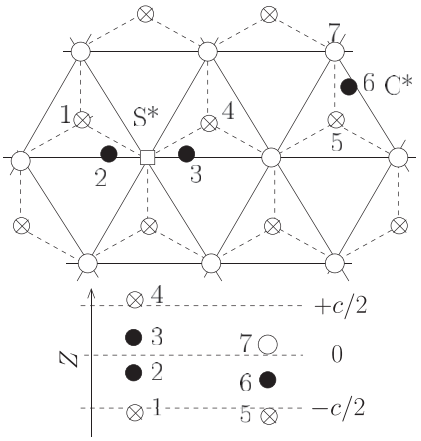

Fig. 4. Basal projection of S* and C* SIAs in Zr. Dashed lines show the hexagonal cross section of the hollow atomic columns of the close packing. Height along axis c is indicated below.

picture of a 1D or 2D migration on the basal plane, was suggested by the earliest DFT simulations using large cells (up to 288 sites) [15]. This was based on the close formation energy predicted for the Bo and Bs configurations. However, later studies also calculating barriers [18,29], have obtained very similar energy for Bo-Bs and Bo-O jumps, $E_m^I \gtrsim 0.25$ eV, slightly favoring the former though. This is consistent with $T_{ID} \approx$ 100 K, and a 3D migration process; the latter is also suggested by our estimated O-Bo jump barrier of 0.15 eV and Table 3 above.

On the other hand, Table 4 gathers our calculated anisotropy ratios, the corresponding defect relaxation volumes, V_r^I (atomic volume units), as well as values from the literature for a sizeably larger supercell [16]. The experimental anisotropy ratio clearly rules out configurations Bo, Bs, and S; this is problematic, because even the most refined calculations, using large supercells (360 sites) and accounting for the elastic interaction between periodic images [18], predict Bo as the most stable SIA, followed by Bs and O at about 0.15 eV higher in energy (from graphs, no table provided). Moreover, an unexpectedly small relaxation volume, $V_r^I = 0.6 \pm 0.15$, was derived in the same experiment by dilatometric measurements, which is incompatible with our results, also implying an unusually small elastic dipole (cf. [6]). Furthermore, the authors [12] had to assume a very small vacancy relaxation volume too, $V_r^V = -0.05$ to -0.10, in order to fit all their data, though this might not affect P_{33}/P_a significantly, our own value being -0.34.

Regarding the IF experiment, on symmetry grounds [30] configurations Bo, O, and S lead to no anelastic relaxation, and Bs (orthorrombic dipole) can show only single peaks, thus all of them must be discarded. Two relaxation frequencies are possible for <100> and <001> monoclinic defects, and even four frequencies for triclinic defects; to our knowledge however, the latter two symmetries have never been reported in the context of DFT calculations in Zr. This lives us with the <100> monoclinic case, of which S*, C*, and C are instances, though the latter is an unlikely candidate due to its high formation energy. Fig. 5 shows the six orientations of a <100> monoclinic dipole projected on the basal plane, together with the two relaxation frequencies, Γ, expanded in terms of elementary defect reorientation frequencies, ν_{ij} [30]. Both relaxation modes should be present for a poly-crystalline sample and, if ν_{14} were dominant, a two-fold IF peak could be observed; unfortunately this is unlikely for either S* or C*. Referring to Fig. 4, one can foresee both configurations turning around the *c* axis, according to a screw-like mechanism, while traversing a flat energy landscape; transition ν_{14} corresponds to configurations located in opposite sides of the dashed hexagons, thus cannot be the fastest process. In summary, none of the simulated SIAs is consistent with the findings of the IF experiment.

Inspection of Fig. 2 suggest that configurations C, S, and S* are the most relevant in Co. The structure of C is much like in Mg, though now there is a noticeable displacement of the nearest neighbors to the crowdion, namely, atoms 4, 5 in Fig. 3 and their inverted images. Also S* possesses a similar structure as in Mg, though here the distortion is shared more evenly between atoms 1 and 7 in Fig. 3. The latter observation supports the idea of an enhanced mobility of atom 2 for roaming within the cage of the octahedral site. Indeed, we evaluated a symmetric configuration, Po, that may serve as barrier for the transition of S* to its mirror image by a vertical $\{11\bar{2}0\}$ plane passing through 6, obtaining $E_f(\mathrm{Po}) - E_f(\mathrm{S}^*) \approx 0.013$ eV. Eventually, S* would connect neighbor cages by recourse to C. Experimentally, recovery stage I occurs in the range $T_{ID} \approx 45 - 60$ K, and interstitial migration energies from 0.1 to 0.15 eV have been estimated by several techniques [6]. The latter is compatible with our calculated $E_f(\mathrm{C}) - E_f(\mathrm{S}) \approx 0.1$ eV; moreover, an anisotropy ratio $P_{33}/P_a = 1.2 \pm 0.1$ has been reported [12], which matches our calculated $P_{33}/P_a = 1.30$ for configuration S, though the P_{ii} themselves resulted about 50% larger than experimental estimations. It is also clear that 3D migration entails the transfer of configuration S between lattice sites, because the above sketched mechanism for S* is essentially 2D. Determination of the barrier for S↔ S* transition turned out to be unreliable; however, by linear interpolation between configurations S and C, and constrained energy minimization on the perpendicular hyper-plane, we found that C may indeed work as barrier for the transition S↔ S connecting non-basal nearest neighbors.

Regarding Cd, there is no quantitative experimental data on individual SIAs; recovery stage I already takes place at $T_{ID} \leqq 3.6$ K and there is evidence of annealing even at 1.5 K [6]. This entails a negligible migration energy that quickly leads to clustering as seen in DXS experiments [12]. On the other hand, it is clear from Fig. 2 and Table 3, that any quantitative differences that may appear among Cd and Zn behavior, cannot be captured by our calculations. Thus the discussion is focused on the latter, where there are more data for SIAs available.

Interstitials in Zn move at very low temperatures ($T_{ID} \approx 13$ K); indeed, some 13% recovery was observed in Ref. [26] after the electron irradiations and before the X-rays measurements at 6 K; moreover, a migration energy $E_m^I = 0.015$ eV was derived from the recovery of resistivity [6]. From Table 3, we obtain O, C, and S* as lowest energy, almost degenerate, SIAs, followed by S some 0,1 eV above. In particular we found no barrier for displacement of O towards C, so that the latter may perform as a barrier of about 0.02 eV in height, for O↔ O transitions within the basal plane. On the other hand, C was found to possess a rather extended structure, with appreciable displacements within ±2 basal planes from the very inversion center, Fig. 6. Finally, S* takes the form of a buckled C

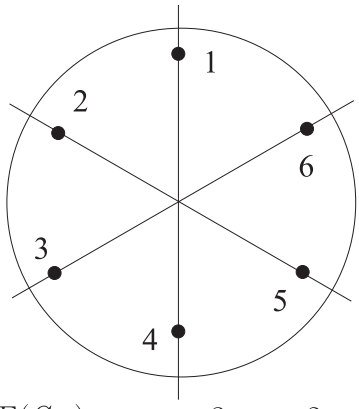

Fig. 5. Orientations of a <100> monoclinic dipole projected on the basal plane and associated compliances relaxation frequencies, $\Gamma(S_{44})$ and $\Gamma(S_{11} - S_{12})$; ν_{ij} are transition probabilities, notice $\nu_{16} = \nu_{12}$ and $\nu_{15} = \nu_{13}$.

Table 4
Calculated and experimental (Exp.) anisotropy ratios and defect relaxation volumes, V_r^I (at. vol.), for Zr.

	O	Bo	C	S	S*	Bs	Exp.[a]
P_{33}/P_a	1.35	0.62	1.27	1.95	1.44	0.48	1.1 ± 0.2
V_r^I	1.23	1.25	1.23	1.17	1.23	1.29	0.6 ± 0.15
P_{33}/P_a [b]	1.17	0.56	1.24	1.93	1.41	0.43	

[a] Ref. [12].
[b] Ref. [16], 288 sites.

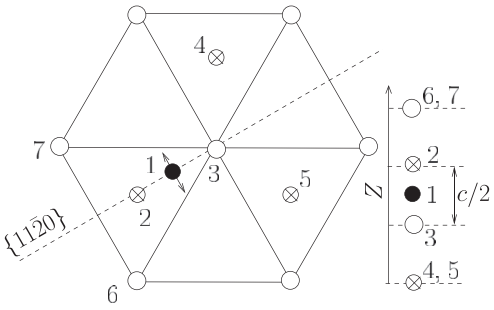

Fig. 6. Most affected atomic neighborhood about a C SIA in Zn, lateral displacement of atom 1 generates configuration S*.

Table 5
Calculated and experimental (Exp.) anisotropy ratios and defect relaxation volumes, V_r^I (at. vol.), for Zn.

	O	C	S	S*	Exp.[a]
P_{33}/P_a	1.39	1.33	1.45	1.33	2.5 ± 0.2
V_r^I	2.91	2.83	2.97	2.84	3.5 ± 0.6

[a] Ref. [12].

(much like C* in Zr) and is also very extended, so that its two mirror images through the {11$\bar{2}$0} plane, together with C, may be conceived as a set of three resonant structures. As in Zr, this complex should be able to migrate very fast connecting near neighbor C sites.

Regarding the elastic dipole, Table 5 compares our calculated anisotropy ratios and relaxation volumes against experimental values [12]; the latter are clearly larger than calculations, most notably for P_{33}/P_a : even our largest value for S is too low when compared to experiment, also attributed to the S interstitial. This is somewhat unexpected, however, because a larger c/a ratio is most likely to be associated with a smaller P_{33}/P_a for S than the converse, cf. Table 4 for Zr. Besides, the experimental findings [26] suggested invariant $\pi^{(2)}$ to be null, result that would rule out C and S*; however this need not be so according to our calculations, that obtained dipoles' off-diagonal components smaller than diagonal ones by at least one order of magnitude. On the other hand, the relaxation volumes are in better agreement with experiment, though still on the low side; also our value for the vacancy, $V_r^V = -0.5$, is somewhat smaller than the experimental −0.6 [6], estimated from the pressure dependence of the diffusion coefficient. In this respect, it is interesting to observe that, if our dipoles are scaled such as to match V_r^V with experiment, meaning that a weaker than an interstitial defect is presumably better calculated, then V_r^I also do match.

Lastly, it is interesting to point that, by analysis of the recovery stage III kinetics, $T_{III} \approx 130 - 155$ K, ref. [31] concludes S to be the involved interstitial, assigning migration energies of 0.34/0.42 eV parallel/perpendicular to the c axis. Even though this may not be at variance with our results, extrapolating the latter to find out the structure of the migrating defect at those relatively high temperatures, remains highly speculative.

4. Summary and conclusions

Overall, we have seen that DFT calculations in hcp metals, provide a consistent picture of SIA structure and migration at low temperatures, in the sense that formation energy differences between SIAs and/or barriers correlate fairly well with the experimental temperatures measured for recovery stage I. Moreover, the relevance of low symmetry, generally overlooked structures, such as S* and C*, as long as they are stable, has also been demonstrated across all the metals here considered. On the other hand, the agreement regarding more specific details, particularly from DXS measurements whenever available, is less clear. This is especially true for Zr, perhaps one of the most thoroughly studied hcp metals, where calculations are strictly not compatible with both, DXS and IF measurements. We believe DFT calculations have already reached a mature, converged, state, so that the situation calls for new experiments, e.g., IF on single crystals and DXS designed to test invariant $\pi^{(2)}$ in particular.

Acknowledgments

The author is grateful to CONICET, subsidy PIP 804/10, for partial support during the course of this research. Also, many thanks to the international community of free software developers.

References

[1] S. Jumel, C. Domain, J. Ruste, J.C.V. Duysen, C. Becquart, A. Legris, P. Pareige, A. Barbu, V. Pontikis, J. Phys. IV Fr. 10 (2000) 191.
[2] S. Leclercq, D. Lidbury, S. Van Dyck, D. Moinereau, A. Alamo, A. Al Mazouzi, J. Nucl. Mater 406 (2010) 193.
[3] L. Malerba, G. Ackland, C. Becquart, G. Bonny, C. Domain, S. Dudarev, C. Fu, D. Hepburn, M. Marinica, P. Olsson, R. Pasianot, J. Raulot, F. Soisson, D. Terentyev, E. Vincent, F. Willaime, J. Nucl. Mater 406 (2010) 7.
[4] S. Han, L.A. Zepeda-Ruiz, G.J. Ackland, R. Car, J. Srolovitz, Phys. Rev. B 66 (22) (2002) 220101.
[5] D. Nguyen-Mahn, A.P. Horsfield, S.L. Dudarev, Phys. Rev. B 73 (2) (2006) 20101.
[6] H. Ullmaier, Atomic Defects in Metals, Landolt-Börstein Series, Group III, vol. 25, Springer, Berlin, 1991.
[7] C.C. Fu, F. Willaime, P. Ordejón, Phys. Rev. Lett. 92 (17) (2004) 175503.
[8] R.C. Pasianot, A.M. Monti, J. Nucl. Mater 264 (1999) 198.
[9] M.S. Daw, M.I. Baskes, Phys. Rev. B 29 (12) (1984) 6443.
[10] R.C. Pasianot, A.M. Monti, G. Simonelli, E.J. Savino, J. Nucl. Mater 276 (2000) 230.
[11] R. Pichon, E. Bisogni, P. Moser, Radiat. Eff. 20 (1973) 159.
[12] P. Ehrhart, B. Schönfeld, in: V. Takamura, J. Doyama, M. Kiritani (Eds.), Proceedings of Yamada Conference on Point Defects and Defect Interactions in Metals, Tokyo University, 1982, p. 47.
[13] C. Domain, A. Legris, Philos. Mag. 85 (4–7) (2005) 569.
[14] G. Kresse, J. Furthmüller, Comp. Mat. Sci. 6 (1996) 15.
[15] Q. Peng, W. Ji, H. Huang, S. De, J. Nucl. Mater 429 (2012) 233.
[16] G. Vérité, C. Domain, C. Fu, P. Gasca, A. Legris, F. Willaime, Phys. Rev. B 87 (2013) 134108.
[17] J.M. Soler, E. Artacho, J.D. Gale, A. García, J. Junquera, P. Ordejón, D. Sánchez-Portal, J. Phys. Condens. Matter 14 (2002) 2745.
[18] C. Varvenne, F. Bruneval, M. Marinica, E. Clouet, Phys. Rev. B 88 (2013) 134102.
[19] P. Blaha, K. Schwarz, P. Sorantin, S. Trickey, Comp. Phys. Comm. 59 (1990) 399.
[20] N. Troullier, J.L. Martins, Phys. Rev. B 43 (3) (1991) 1993.
[21] J.P. Perdew, K. Burke, M. Ernzerhof, Phys. Rev. Lett. 77 (18) (1996) 3865.
[22] R.C. Pasianot, R.A. Pérez, V.P. Ramunni, M. Weissmann, J. Nucl. Mater 392 (2009) 100.
[23] R.C. Pasianot, R.A. Pérez, Phys. B 407 (2012) 3298.
[24] R.C. Pasianot, R.A. Pérez, J. Nucl. Mater 434 (2013) 158.
[25] V.P. Ramunni, M.A. Alurralde, R.C. Pasianot, Phys. Rev. B 74 (5) (2006) 54113.
[26] P. Ehrhart, B. Schönfeld, Phys. Rev. B 19 (8) (1979) 3896.
[27] M.G. Ganchenkova, P.V. Vladimirov, V.A. Borodin, J. Nucl. Mater 386–388 (2009) 79.
[28] G.M. Hood, J. Nucl. Mater 159 (1988) 149.
[29] G.D. Samolyuk, A.V. Barashev, S.I. Golubov, Y.N. Osetsky, R. E Stoller, Acta Mater 78 (2014) 173.
[30] A.S. Nowick, Adv. Phys. 16 (61) (1967) 1.
[31] A. Seeger, Philos. Mag. A 64 (1991) 735.